# Rapidity and centrality dependence of particle production for identified hadrons in Cu + Cu collisions at $\sqrt{s_{NN}} = 200$ GeV

I. C. Arsene,[11] I. G. Bearden,[6] D. Beavis,[1] S. Bekele,[10,*] C. Besliu,[9] B. Budick,[5] H. Bøggild,[6] C. Chasman,[1] C. H. Christensen,[6] P. Christiansen,[6,†] H. H. Dalsgaard,[6] R. Debbe,[1] J. J. Gaardhøje,[6] K. Hagel,[7] H. Ito,[1] A. Jipa,[9] E. B. Johnson,[10,‡] C. E. Jørgensen,[6,§] R. Karabowicz,[4] N. Katrynska,[4] E. J. Kim,[10,‖] T. M. Larsen,[6] J. H. Lee,[1] G. Løvhøiden,[11] Z. Majka,[4] M. J. Murray,[10] J. Natowitz,[7] B. S. Nielsen,[6] C. Nygaard,[6] D. Pal,[10] A. Qviller,[11] F. Rami,[2] C. Ristea,[3] O. Ristea,[9] D. Röhrich,[8] S. J. Sanders,[10] P. Staszel,[4] T. S. Tveter,[11] F. Videbæk,[1] R. Wada,[7,¶] H. Yang,[8] Z. Yin,[8,#] and I. S. Zgura[3]
(BRAHMS Collaboration)

[1]*Brookhaven National Laboratory, Upton, New York 11973, USA*
[2]*Institute Pluridisciplinaire Hubert Curien CRNS-IN2P3 et Université de Strasbourg, F-67037 Strasbourg, France*
[3]*Institute for Space Sciences, RO-077125 Bucharest, Romania*
[4]*Smoluchowski Institute of Physics, Jagiellonian University, PL-30348 Krakow, Poland*
[5]*Department of Physics, New York University, New York 10003, USA*
[6]*Niels Bohr Institute, Blegdamsvej 17, University of Copenhagen, DK-2100 Copenhagen 2100, Denmark*
[7]*Cyclotron Institute, Texas A&M University, College Station, Texas 77843, USA*
[8]*Department of Physics and Technology, University of Bergen, N-5020 Bergen, Norway*
[9]*Faculty of Physics, University of Bucharest, RO-077125 Bucharest, Romania*
[10]*Department of Physics & Astronomy, University of Kansas, Lawrence, Kansas 66045, USA*
[11]*Department of Physics, University of Oslo, N-0316 Oslo, Norway*

(Received 3 February 2016; revised manuscript received 12 May 2016; published 20 July 2016)

The BRAHMS collaboration has measured transverse momentum spectra of pions, kaons, protons, and antiprotons at rapidities 0 and 3 for Cu+Cu collisions at $\sqrt{s_{NN}} = 200$ GeV. As the collisions become more central the collective radial flow increases while the temperature of kinetic freeze-out decreases. The temperature is lower and the radial flow weaker at forward rapidity. Pion and kaon yields with transverse momenta between 1.5 and 2.5 GeV/$c$ are suppressed for central collisions relative to scaled $p + p$ collisions. This suppression, which increases as the collisions become more central, is consistent with jet quenching models and is also present with comparable magnitude at forward rapidity. At such rapidities, initial state effects may also be present and persistence of the meson suppression to high rapidity may reflect a combination of jet quenching and nuclear shadowing. The ratio of protons to mesons increases as the collisions become more central and is largest at forward rapidities.

DOI: 10.1103/PhysRevC.94.014907

## I. INTRODUCTION

The Relativistic Heavy Ion Collider (RHIC) collides nuclei as heavy as gold or uranium with center-of-mass energies up to 200 GeV per nucleon. Such collisions produce extended, strongly coupled, opaque, partonic systems that exhibit hydrodynamic flow. This quantum fluid has a viscosity to entropy ratio near the theoretical lower limit [1] and is known as the strongly coupled quark gluon plasma or sQGP [2–5].

The matter created in heavy-ion collisions exists for a very short period of time. After the collision it expands and cools down with the subsequent hadronization of all partons, some of which are eventually detected by the experiments as jets or leading hadrons. The medium can be explored by comparing spectra of hard probes from heavy-ion collisions (where the partons have to traverse an extended medium) to those of a smaller system, such as $p + p$ collisions, at the same energy per nucleon. Jet and leading hadron measurements are believed to probe the early stages of the dense medium while soft hadronic observables deliver information on the initial state and hydrodynamic evolution of the system.

The systematic study of such observables, as a function of the number of participants in the collisions $N_{\text{part}}$, was very important in understanding the matter created in Au+Au collisions at $\sqrt{s_{NN}} = 200$ GeV. However, for peripheral Au+Au collisions with $N_{\text{part}} < 60$ the uncertainties on $N_{\text{part}}$ are of the order of 20% [6,7] leaving room for different scenarios for the dependence of particle production on the system size.

To extend the medium size dependence of physical observables down to small systems such as d+Au and $p + p$, the Cu+Cu system, with $A_{Cu} = 63$, was selected because it provides a good overlap with peripheral Au+Au collisions in terms of the number of participants. The relative uncertainty in the fractional cross section of Cu+Cu collisions is smaller compared to that in Au+Au collisions for the same number

[*]Present address: Dept. of Polymer Science, The University of Akron, Akron, Ohio.
[†]Present Address: Div. of Experimental High-Energy Physics, Lund University, Lund, Sweden.
[‡]Present Address: Radiation Monitoring Devices, Cambridge, MA, USA.
[§]Present address: Risø National Laboratory, Denmark.
[‖]Present address: Division of Science Education, Chonbuk National University, Jeonju, 561-756, Korea.
[¶]Present address: Institute of Modern Physics, Chinese Academy of Sciences, Lanzhou, China.
[#]Present address: Huazhong Normal University,Wuhan, China.

 

of participants. Assuming a uniform mass distribution, the overlap region in central Cu+Cu collisions is spherical while that in Au+Au collisions for the same number of participants has an almond shape, making it possible to explore geometry effects on the experimental observables. The core-corona model of K. Werner [8] and Beccattini and Manninen [9] provides a mechanism for testing these effects because the ratio of core to corona depends upon the shape of the overlap region.

Most available data of identified hadrons are from near mid-rapidity. The BRAHMS data offers a unique opportunity to study hadron production at both mid- and forward rapidity and compare properties to further enhance our knowledge of the matter formed and different chemical conditions. The $p_T$ spectra of charged hadrons, $(\pi^{\pm}, K^{\pm}, p, \bar{p})$, from Cu+Cu collisions at $\sqrt{s_{NN}} = 200$ GeV were measured at $y = 0$ and $y = 3$ as a function of collision centrality. The results are compared to those obtained in $p + p$ and Au+Au collisions at the same energy, rapidity and centrality (number of participants) where available.

In elementary $p + p$ and $\bar{p} + p$ collisions the hadron spectra can be described by perturbative QCD for $p_{\mathrm{T}}$ above $\approx$2 GeV [10–12]. The Cu+Cu data presented in this paper cover the region of soft physics and the transition to high-$p_{\mathrm{T}}$ phenomena. In this paper we seek to follow this transition by first studying the global hydrodynamic properties of the system using Blast Wave fits, second presenting the total yields and mean transverse momenta $\langle p_T \rangle$ for each particle type, third showing the ratios of different particles as a function of $p_{\mathrm{T}}$ and finally focusing on the nuclear modification factors ($R_{AA}$) as a function of $p_{\mathrm{T}}$ and rapidity.

## II. THE BRAHMS EXPERIMENT

The BRAHMS experiment consists of two small acceptance magnetic spectrometers, the mid-rapidity spectrometer (MRS) and the forward spectrometer (FS), for tracking, momentum determination, and particle identification together with a system of global detectors made up of beam-beam counters (BBC), zero degree calorimeters (ZDCs), and a multiplicity array (MA) [13,14]. The global detectors are used for triggering, centrality determination, and separating nuclear from electromagnetic events. The MRS uses two time projection chambers (TPCs), TPM1 and TPM2, with a magnet between them and time-of-flight (TOF) walls for particle identification (PID). The forward spectrometer (FS) has two TPCs (T1 and T2) and three drift chambers (DCs) with magnets located between the detectors. In the FS, PID is achieved by using a TOF wall behind T2 and a second TOF wall and a ring imaging Cherenkov (RICH) detector both placed after the third DC [15]. The TPCs and DCs each provide several three-dimensional space points which together with the momentum information provided by the deflection in magnets allow for particle tracking. The MRS is capable of rotating between 90° and 30° with respect to the beam pipe covering the rapidity interval from $y \sim 0$ to $y \sim 1.6$. The FS rotates between 15° and 2° and covers the rapidity interval from $y \sim 2.2$ to $y \sim 4.0$. For the data presented in this paper, the MRS was set at 90° and the FS was set at 4°. These settings correspond to $y = 0$ and $y = 3$, respectively.

TABLE I. $\langle N_{\mathrm{part}} \rangle$ and $\langle N_{\mathrm{coll}} \rangle$ for the centrality ranges used for Cu+Cu in this paper. Note the errors are correlated between different centrality values.

| Cent. | $\langle N_{\mathrm{part}} \rangle$ | $\langle N_{\mathrm{coll}} \rangle$ |
|---|---|---|
| 0%–10% | $97 \pm 0.8$ | $166 \pm 2$ |
| 10%–30% | $61 \pm 2.6$ | $85 \pm 5$ |
| 30%–50% | $29 \pm 4.3$ | $30 \pm 6$ |
| 50%–70% | $12 \pm 3.2$ | $9.6 \pm 3.2$ |

The primary collision vertex position is determined to an accuracy of ~1 cm based on the relative time of flight of fast ($\beta \approx 1$) particles hitting the beam-beam counter arrays (BBC). The BBCs consist of Cherenkov detectors mounted on photomultiplier tubes and are located 220 cm from the nominal vertex position on either side of the interaction region. The BBCs also provide the start time for the time-of-flight measurements.

### A. Event selection

The centrality of the collisions is characterized by using a multiplicity array (MA), which consists of an inner layer of Si strip detectors and an outer layer of scintillator tiles each arranged as hexagonal barrels coaxial with the beam pipe. By measuring the energy loss of charged particles that traverse the two arrays, the strip detectors and the tiles provide two semi-independent measurements from which the pseudorapidity dependence of the charged particle density can be deduced. A detailed GEANT3 simulation of the detector response is used in this determination to map energy deposits to the corresponding number of primary particles [16]. Reaction centrality is based on the distribution of charged particle multiplicities within the nominal pseudorapidity range covered by the MA, $|\eta| < 2.2$.

For a given event the centrality was taken to be defined as the fraction of observed events with a greater charged particle multiplicity than that event. Using this definition, 0% centrality corresponds to collisions with the greatest overlap of the two nuclei. Events generated by HIJING were passed through a GEANT3 simulation of the experiment and used to estimate the number of peripheral events missed because they do not leave sufficient energy in the MA for detection. The procedure applied for determining centrality and the associated numbers of participants $\langle N_{\mathrm{part}} \rangle$, and binary nucleon-nucleon collisions $\langle N_{\mathrm{coll}} \rangle$ in the Cu+Cu system is the same as described in detail for the Au+Au analysis [17]. The values extracted from this procedure are displayed in Table I.

For this analysis, the events were divided into four centrality classes (0%–10%,10%–30%, 30%–50%, and 50%–70%). Events within ±25 cm of the nominal vertex were selected. Because the spectrometer acceptance depends upon the location of the vertex for a given event, spectral analysis is carried out in vertex bins of 5 cm and the results are statistically averaged to obtain the final spectra.

### B. Track selection

Straight line track segments are determined by tracking detectors, which are outside the magnetic field regions. These track segments are joined inside the analyzing magnet by taking an effective edge approximation. Matching track segments before and after the analyzing magnets allows for the determination of the track's momentum using the vertical magnetic field, the length traversed in the magnetic field region and the orientation of the incoming and outgoing tracks.

Once the momentum is known, the reconstructed tracks are projected toward the beam axis and checked for consistency with the collision vertex determined by the BBCs. A $3\sigma$ cut is applied about the mean of the distribution of differences between the projected track vertex and the BBC vertex along the beam direction. An elliptical cut of $3\sigma$ is applied to the two-dimensional distributions of track intersections with the primary vertex plane. This plane is defined as the plane normal to the beam axis that contains the collision vertex. The rapidity cuts were $|y| < 0.1$ at midrapidity and $2.95 < y < 3.15$ at forward rapidity.

### C. Particle identification

In this analysis, the MRS time of flight and the FS RICH detectors are used for PID at $y = 0$ and $y = 3$, respectively. The time-of-flight measurement with TOFW and knowledge of the flight path length allows $\beta$ to be determined. This together with the momentum of a detected particle provides for particle identification using the relation,

$$\frac{1}{\beta^2} = \frac{m^2}{p^2} + 1. \tag{1}$$

Particles of different masses fall on separate curves if $\frac{1}{\beta}$ is plotted versus momentum. The TOFW provides $\pi/K$ separation up to a momentum of 2 GeV/$c$ and $K/p$ separation up to 3 GeV/$c$. Figure 1 (top) shows the distribution of $\frac{1}{\beta}$ vs $p$ for the MRS where $q = 1$ for positive particles and $q = -1$ for negative particles. For this analysis, tracks were required to have measured $\frac{1}{\beta}$ values within $3\sigma$ of the nominal values given by Eq. (1) for each particle species. The curves show the $3\sigma$ cuts around the nominal trajectories for the different particle species.

For the FS, the emission angle $\theta_c$ of the light radiated in the RICH detector along the particle path is given by

$$\cos\theta_c = \frac{1}{n\beta}, \tag{2}$$

where $n$ is the index of refraction of the gas inside the RICH volume. A spherical mirror of focal length $L$ was used to focus the light cones onto rings of radii,

$$r = L\tan\theta_c. \tag{3}$$

Once the radii of the Cherenkov rings are measured, the masses of the particles are deduced from the formula,

$$r = L\tan\left[\cos^{-1}\left(\frac{1}{n}\sqrt{1+\frac{m^2}{p^2}}\right)\right]. \tag{4}$$

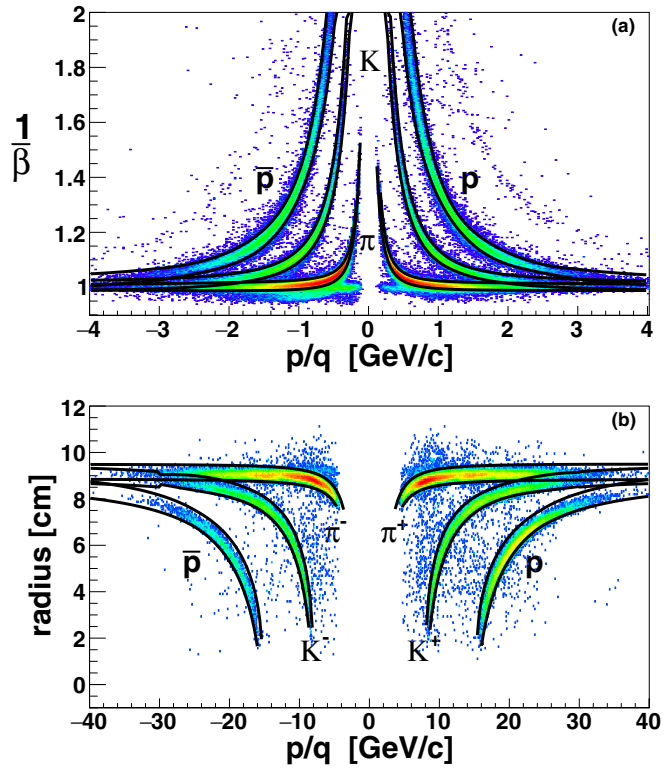


FIG. 1. Scatter plots of $\frac{1}{\beta}$ versus $p/q$ (top) and RICH radius versus $p/q$ (bottom) for Cu+Cu collisions at $\sqrt{s_{NN}} = 200$ GeV. The solid curves show the $3\sigma$ cuts around the nominal values given by Eqs. (1) and (4).

The RICH can identify pions starting at 2.5 GeV/$c$, kaons starting around 8 GeV/$c$, and protons (antiprotons) from 15 GeV/$c$. The $\pi/K$ $3\sigma$ separation extends up to 20 GeV/$c$ and protons (antiprotons) can be identified up to 35 GeV/$c$. Figure 1 (bottom) shows the distribution of radius $r$ vs $p$ for the RICH detector. At $y = 3$, the tracks were required to have a RICH radius within $3\sigma$ of the nominal radius for a given species as determined from Eq. (4), with a correction to the yield applied for purity in the overlap regions.

### D. Corrections

The data presented are corrected for the geometrical acceptance of the spectrometers, tracking efficiency, particle misidentification, and the effects of particle decays based on the GEANT3 simulations. These simulations are also used to correct the experimental results for effects such as interactions with the beam pipe, absorption, and multiple scattering within the gas volumes of the tracking detectors.

To account for the acceptance, particles are generated with a uniform momentum distribution over a range of angles $\Delta\phi$ and $\Delta\theta$ broad enough for the spectrometer aperture to lie within the range. The acceptance factor for a given pseudorapidity and $p_T$ range is then the fraction of accepted particles to those thrown scaled by $\frac{\Delta\phi}{2\pi}$. This is done for each vertex bin and for the different spectrometer angle and magnetic field settings. The acceptance correction is applied to the individual spectra from different spectrometer settings before they are averaged.

TABLE II. Purity estimates of the pion and kaon raw spectra, $c_{\mathrm{PID}}$, and their relative systematic uncertainties for pions and kaons at central and forward rapidity for various values of the total momenta. As an example the raw pion spectrum at 2.25 GeV/$c$ is corrected by a factor of $0.85 \pm 0.01$.

| | $y = 0$ | | $y = 3$ | |
|---|---|---|---|---|
| P | 1.5 GeV | 2.25 GeV | 24 GeV | 30 GeV |
| $\pi$ | >99% | $85\% \pm 1\%$ | >99% | $88\% \pm 5\%$ |
| K | >99% | $50\% \pm 5\%$ | >99% | 65%–70% $\pm 5\%$ |

The tracking efficiency is calculated by a data driven method, using a reference tracks method where good tracks from one set of detectors are taken as input to a detector whose efficiency is sought. For the MRS, for example, tracks from the first time projection chamber (TPC) and the time-of-flight wall are used as input to determine the efficiency for the second TPC, and *vice versa*. The ratio of the number of tracks matching the reference tracks to the total number of input reference tracks is taken as the tracking efficiency. The product of the efficiencies calculated for the two MRS TPCs in this way is then taken to be the overall tracking efficiency for the MRS and is ∼92%. In the FS the tracking efficiencies were determined as a function of spectrometer setting, centrality, and position in the T1–T5 chambers. The efficiencies are uniformly in $p_{\mathrm{T}}$ above 98% for T2–T4, and only for T1 with the higher track density is there a weak centrality dependence. No dependence of the tracking efficiencies on the particle species is observed. The systematic error on the tracking efficiencies is small, less than 2%, and determined by varying cuts for track and matching selection. For the FS, the overall tracking efficiency is ∼80%, determined as the product of the individual efficiencies for all tracking stations.

The corrections for multiple scattering and hadronic absorption were computed by simulating single-particle events with GEANT3 (including the relevant physical processes in the detector material) and processing the results through the standard BRAHMS analysis code. The simulations included multiple scattering and hadronic interaction processes. These GEANT corrections are applied on a track-by-track basis for both the MRS and FS.

To take into account particle misidentification, a PID correction was applied to the pion and kaon spectra. At higher momenta the well-defined $3\sigma$ bands start to overlap. The contamination of the pions and kaons was evaluated by fitting the distributions in $\mathrm{m}^2$, $\frac{1}{\beta}$ or ring radius for narrow $p_T$ bins and determining the contamination fractions and their systematic uncertainties. The invariant yields have been corrected because of this effect. Typical correction factors are given in Table II. In the momentum range covered, the (anti)protons are well separated from the mesons and no PID correction is applied to their spectra.

The overlapping rapidity and $p_T$ acceptance of different momentum and angular settings of the spectrometer make it possible to estimate the systematic uncertainties on the final spectra associated with the determination of the tracking efficiency, merging of different spectrometer settings, and normalization [13] by comparing spectra from different settings. These systematic errors are found to be between ∼5%–8%.

Feed down from Λ-decay corrections is not applied to the proton (antiproton) spectra. This is primarily because the spectra of Λ's have not been measured at the higher rapidities. Later, when discussing integrated yields ($dN/dy$) of protons at mid-rapidity, those have been corrected to first order because the Λ yields were measured by other experiments [18,19]. The detailed GEANT simulations indicate that in the MRS about 90% of the decay protons from Λs are reconstructed as primary particles. This fraction drops to 80% in the FS [20]. These simulations assumed that the Λ spectra are exponential in $p_{\mathrm{T}}$ with an inverse slope deduced from measurements by STAR and PHENIX, [21,22]. The fraction of protons from weak decays varies from 0.38 to 0.22 as the momentum of the particle increases from 0.5 to 3.0 GeV/c [23]. Both Λs and $K^0_S$ produce pions that may be reconstructed as primary particles. For the mid-rapidity and forward spectrometers about 5% and 7%, respectively, of the measured pion yield is from such weak decays [20].

## III. RESULTS AND DISCUSSION

### A. Particle spectra

Measurement of transverse momenta spectra is the crucial first step in obtaining the various observables used to characterize the properties of the partonic medium created in heavy-ion collisions. Figure 2 shows the invariant spectra for the charged hadrons $\pi^{\pm}, K^{\pm}, p$, and $\bar{p}$, versus transverse kinetic energy, for different collision centralities at $y = 0$ and $y = 3$. The spectra of particles and antiparticles have very similar shapes. Comparing pions, kaons, and protons, a steady hardening of the spectra with particle mass is observed. Both of these effects are suggestive of hydrodynamics. The lines in Fig. 2 are fits of the hydrodynamical inspired blast wave model [24] to the six $\pi^{\pm}, K^{\pm}, p$, and $\bar{p}$ spectra at a given rapidity and centrality. These fits will be discussed in detail later. The magnitudes of the spectra depend strongly on centrality for all particles and for both rapidities. For kaons and protons the shapes of the spectra harden as one moves from peripheral to central collisions. The spectra for all particle species are softer at forward rapidity but, again, one observes a strong centrality dependence.

A systematic study of the spectra was performed by fitting them to a variety of functions. For pions the Levy function $A(1 + \frac{(m_T - m_0)}{n_0 T})^{-n_0}$ [25–27] provided the best fit to the data. For kaons and protons the spectra were best fit by an exponential function in $m_T$, $Ae^{-\frac{m_T}{T}}$, but fits to a Boltzman function, $Am_T e^{-\frac{m_T}{T}}$, were also good. For the Boltzmann function, the fit parameter $T$ can be thought of as the effective temperature of the system. The $p_{\mathrm{T}}$ range used for the Levy fits is much larger than for the blast wave fits to better determine the pion yields and $\langle p_T \rangle$.

The weights used in the fitting procedure are the quadratic sum of the statistical errors and the point-to-point systematic errors. The fit range, fit parameters, number of degrees of freedom, NDF, and $\chi^2$/NDF, are listed in Tables III–V for pions, kaons, and protons, respectively. The integrated yields

TABLE III. Extracted fit results for pions based on a Levy function. The fitting range is 0.35 GeV/$c$ < $p_T$ < 2.0 GeV/$c$ at $y = 0$ and 0.45 GeV/$c$ < $p_T$ < 2.0 GeV/$c$ at $y = 3$. The systematic uncertainties are dominated by the extrapolation to $p_T = 0$.

| | | Cent. | $\frac{dN}{dy}$ | $(\frac{dN}{dy})_m$ | $\frac{N_m}{N}$ | $\langle p_T \rangle$ (MeV) | $\frac{\chi^2}{\text{d.o.f}}$ | $n_0$ | $T$ (MeV) |
|---|---|---|---|---|---|---|---|---|---|
| $\pi^+$ | $y = 0$ | 0%–10% | 81.1 ± 3.1 ± 5.9 | 42.1 | 0.52 | 454 ± 2 ± 21 | 0.2/9 | 12.8 | 172 |
| | | 10%–30% | 48.0 ± 2.1 ± 3.5 | 24.3 | 0.51 | 445 ± 4 ± 21 | 0.9/9 | 11.6 | 164 |
| | | 30%–50% | 21.8 ± 0.5 ± 1.6 | 10.8 | 0.50 | 438 ± 2 ± 21 | 0.2/9 | 11.2 | 159 |
| | | 50%–70% | 8.5 ± 0.40 ± 0.62 | 4.0 | 0.47 | 418 ± 5 ± 20 | 2.4/9 | 10.2 | 147 |
| | $y = 3$ | 0%–10% | 33.7 ± 3.5 ± 3.0 | 11.2 | 0.33 | 401 ± 8 ± 26 | 12.2/9 | 17.0 | 159 |
| | | 10%–30% | 18.3 ± 1.9 ± 1.6 | 6.6 | 0.36 | 424 ± 9 ± 28 | 16.2/9 | 19.3 | 173 |
| | | 30%–50% | 9.3 ± 0.88 ± 0.83 | 3.1 | 0.33 | 403 ± 7 ± 26 | 7.3/9 | 16.1 | 158 |
| | | 50%–70% | 3.3 ± 0.70 ± 0.29 | 1.2 | 0.35 | 418 ± 14 ± 27 | 23.0/9 | 17.9 | 168 |
| $\pi^-$ | $y = 0$ | 0%–10% | 78.0 ± 3.3 ± 4.9 | 41.1 | 0.53 | 460 ± 4 ± 22 | 0.9/9 | 13.3 | 176 |
| | | 10%–30% | 44.7 ± 1.9 ± 2.8 | 23.2 | 0.52 | 455 ± 5 ± 21 | 2.1/9 | 12.3 | 170 |
| | | 30%–50% | 20.5 ± 0.9 ± 1.3 | 10.2 | 0.50 | 441 ± 3 ± 21 | 0.5/9 | 10.6 | 158 |
| | | 50%–70% | 8.0 ± 0.36 ± 0.51 | 3.8 | 0.47 | 421 ± 4 ± 20 | 0.7/9 | 10.2 | 148 |
| | $y = 3$ | 0%–10% | 32.4 ± 3.1 ± 2.9 | 11.2 | 0.35 | 411 ± 8 ± 27 | 14.5/9 | 17.5 | 164 |
| | | 10%–30% | 20.8 ± 1.8 ± 1.8 | 7.4 | 0.36 | 419 ± 8 ± 27 | 13.9/9 | 21.0 | 173 |
| | | 30%–50% | 11.1 ± 1.4 ± 1.0 | 3.5 | 0.32 | 392 ± 9 ± 25 | 16.8/9 | 15.5 | 152 |
| | | 50%–70% | 3.6 ± 0.40 ± 0.32 | 1.3 | 0.36 | 424 ± 8 ± 28 | 5.2/9 | 20.5 | 174 |

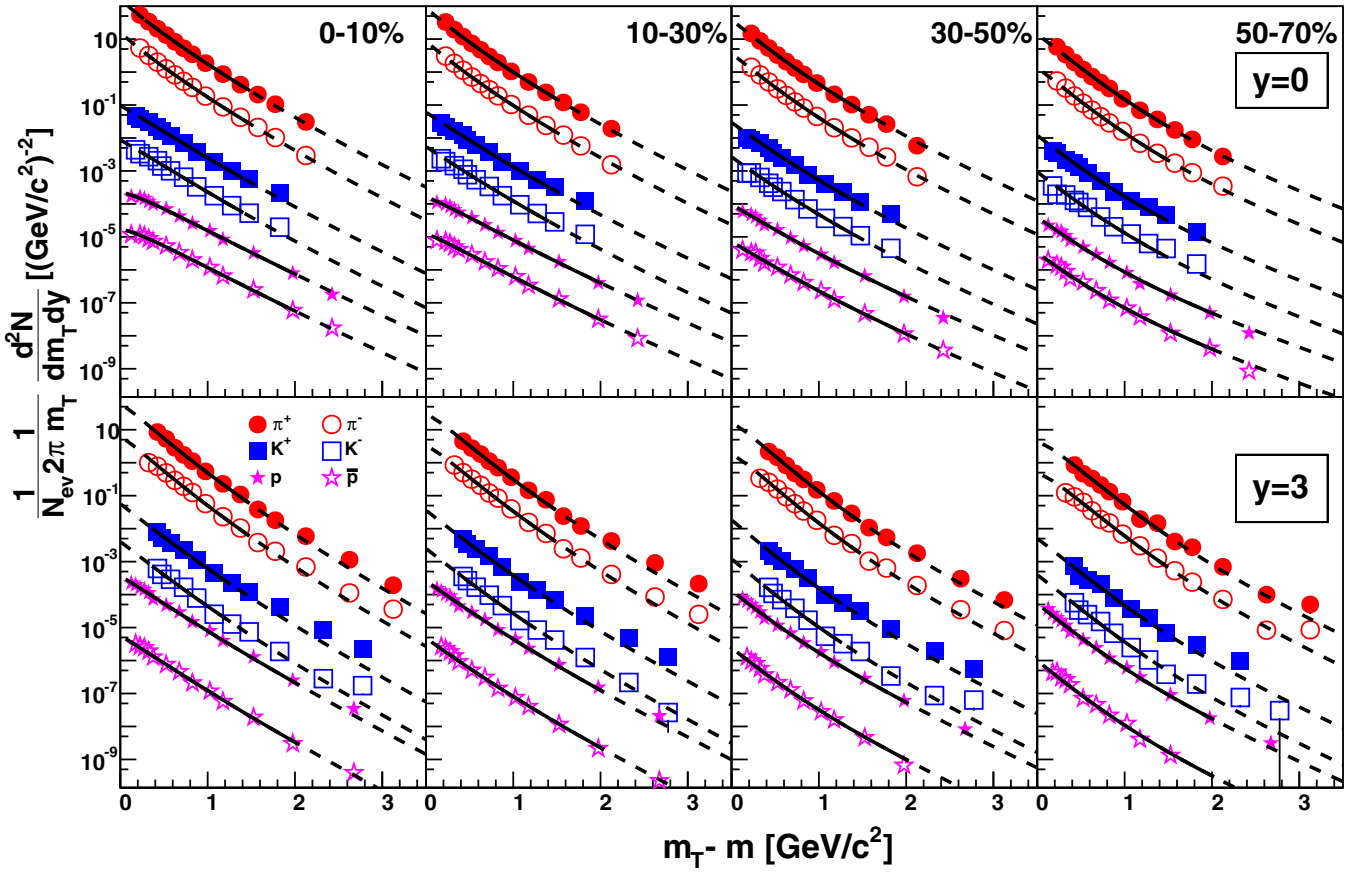


FIG. 2. Invariant spectra from Cu+Cu collisions at $\sqrt{s_{NN}} = 200$ GeV versus transverse kinetic energy at $y = 0$ (top panels) and $y = 3$ (bottom panels) as a function of centrality for $\pi^{\pm}, K^{\pm}, p$, and $\bar{p}$. The $\pi^-, K^+, K^-, p$, and $\bar{p}$ spectra are scaled by factors of $10^{-1}, 10^{-2}, 10^{-3}, 10^{-4}$, and $10^{-5}$, respectively. The lines show the results of blast wave fits to each of the six spectra at a given rapidity and centrality. The solid lines indicate the fit range used while the dashed lines are extrapolations of the functions beyond the fit range. Only the statistical errors are shown because the point-to-point systematic errors are of the order of 5%–8% and are smaller than the size of the symbols.

TABLE IV. Extracted fit results for kaons based on an exponential function in $m_T$. The fitting range is 0.45 GeV/$c$ < $p_T$ < 2.0 GeV/$c$ at $y = 0$ and 0.75 GeV/$c$ < $p_T$ < 2.5 GeV/$c$ at $y = 3$.

| | | Cent. | $\frac{dN}{dy}$ | $(\frac{dN}{dy})_m$ | $\frac{N_m}{N}$ | $\langle p_T \rangle$ (MeV) | $\frac{\chi^2}{\text{d.o.f}}$ | $T$ (MeV) |
|---|---|---|---|---|---|---|---|---|
| $K^+$ | $y = 0$ | 0%–10% | 12.3 ± 0.32 ± 0.89 | 7.6 | 0.62 | 674 ± 10 ± 22 | 1.6/7 | 277 |
| | | 10%–30% | 6.9 ± 0.01 ± 0.50 | 4.2 | 0.61 | 663 ± 7 ± 21 | 0.9/7 | 271 |
| | | 30%–50% | 2.8 ± 0.02 ± 0.20 | 1.7 | 0.62 | 667 ± 14 ± 21 | 3.9/7 | 273 |
| | | 50%–70% | 1.0 ± 0.05 ± 0.12 | 0.6 | 0.59 | 625 ± 14 ± 20 | 3.4/7 | 251 |
| | $y = 3$ | 0%–10% | 4.6 ± 0.29 ± 0.36 | 1.3 | 0.27 | 611 ± 14 ± 20 | 4.1/4 | 244 |
| | | 10%–30% | 3.0 ± 0.20 ± 0.23 | 0.78 | 0.26 | 594 ± 19 ± 19 | 5.8/4 | 235 |
| | | 30%–50% | 1.4 ± 0.11 ± 0.11 | 0.34 | 0.25 | 577 ± 20 ± 18 | 5.7/4 | 226 |
| | | 50%–70% | 0.39 ± 0.05 ± 0.03 | 0.10 | 0.26 | 600 ± 27 ± 19 | 5.4/4 | 238 |
| $K^-$ | $y = 0$ | 0%–10% | 11.2 ± 0.23 ± 0.71 | 7.2 | 0.64 | 682 ± 9 ± 22 | 2.0/8 | 282 |
| | | 10%–30% | 6.1 ± 0.15 ± 0.38 | 3.9 | 0.64 | 683 ± 12 ± 22 | 4.3/8 | 282 |
| | | 30%–50% | 2.5 ± 0.08 ± 0.16 | 1.6 | 0.63 | 677 ± 26 ± 22 | 11.4/8 | 279 |
| | | 50%–70% | 0.7 ± 0.02 ± 0.10 | 0.5 | 0.64 | 685 ± 28 ± 22 | 10.8/8 | 283 |
| | $y = 3$ | 0%–10% | 3.9 ± 0.02 ± 0.30 | 0.96 | 0.25 | 569 ± 12 ± 18 | 5.4/5 | 222 |
| | | 10%–30% | 2.2 ± 0.12 ± 0.17 | 0.57 | 0.26 | 580 ± 10 ± 19 | 4.4/5 | 227 |
| | | 30%–50% | 1.0 ± 0.05 ± 0.08 | 0.24 | 0.23 | 551 ± 12 ± 18 | 4.8/5 | 213 |
| | | 50%–70% | 0.34 ± 0.02 ± 0.03 | 0.08 | 0.25 | 572 ± 12 ± 18 | 1.5/5 | 223 |

$\frac{dN}{dy}$, and mean transverse momenta $\langle p_T \rangle$, are obtained by extrapolating the fit functions outside the measurement region.

The dominant uncertainties on $\frac{dN}{dy}$ and $\langle p_T \rangle$ result from the extrapolation of the spectra to $p_T = 0$. They were estimated by varying the functional form and $p_T$ range of the fits. The set of fits which had a reasonable $\chi^2$ were then used to estimate the systematic errors. For pions and kaons the extrapolation to $p_T = 0$ is more significant at $y = 3$ than at $y = 0$ because the lower limit of the $p_T$ range is higher than at $y = 3$. This effect increases the systematic uncertainties on the forward spectra. The fraction of the particle yield within the BRAHMS acceptance varies from 30%–75% depending upon the spectrometer setting and particle species.

A model-dependent analysis of the transverse momentum spectra as a function of rapidity and centrality allows the extraction of the thermodynamic and collective properties of the system at kinetic freeze-out. At mid-rapidity the hydro-inspired blast wave model [24] predicts a spectrum with

$$\frac{dN}{m_T dm_T} \sim \int_0^{R_{\max}} dr\{r \times n(r) \times [m_T I_0(x) K_1(z)]\}, \quad (5)$$

where $x = \frac{p_T}{T_{\text{kin}}} \sinh(\rho)$, $z = \frac{m_T}{T_{\text{kin}}} \cosh(\rho)$, $\rho = \tanh^{-1}(\beta_T)$, and $\beta_T(r) = \beta_s(\frac{r}{R})^\alpha$ is the velocity profile as a function of radial distance $r$. In this model $T_{\text{kin}}$ represents the kinetic temperature of the system, $\beta_s$ the velocity of the surface of the expanding medium, and $\alpha$ controls how the velocity of the expanding matter depends upon radial distance. For this study $R$ was taken

TABLE V. Extracted fit results for protons and antiprotons based on an exponential function in $m_T$. The fitting range is 0.55 GeV/$c$ < $p_T$ < 2.0 GeV/$c$ at $y = 0$ and 0.45 GeV/$c$ < $p_T$ < 2.5 GeV/$c$ at $y = 3$.

| | | Cent. | $\frac{dN}{dy}$ | $(\frac{dN}{dy})_m$ | $\frac{N_m}{N}$ | $\langle p_T \rangle$ (MeV/$c$) | $\frac{\chi^2}{\text{d.o.f}}$ | $T$ (MeV) |
|---|---|---|---|---|---|---|---|---|
| $p$ | $y = 0$ | 0%–10% | 8.1 ± 0.03 ± 0.51 | 5.7 | 0.70 | 896 ± 18 ± 29 | 9.1/9 | 332 |
| | | 10%–30% | 4.7 ± 0.10 ± 0.29 | 3.2 | 0.69 | 874 ± 9 ± 28 | 1.9/9 | 320 |
| | | 30%–50% | 2.1 ± 0.05 ± 0.13 | 1.4 | 0.67 | 831 ± 14 ± 27 | 6.4/9 | 296 |
| | | 50%–70% | 0.7 ± 0.03 ± 0.05 | 0.46 | 0.64 | 784 ± 25 ± 25 | 12.3/9 | 271 |
| | $y = 3$ | 0%–10% | 7.0 ± 0.03 ± 0.44 | 5.1 | 0.74 | 775 ± 13 ± 25 | 10.3/10 | 266 |
| | | 10%–30% | 4.3 ± 0.11 ± 0.27 | 3.2 | 0.73 | 761 ± 16 ± 24 | 12.4/10 | 259 |
| | | 30%–50% | 2.0 ± 0.07 ± 0.12 | 1.4 | 0.71 | 737 ± 38 ± 24 | 23.2/10 | 247 |
| | | 50%–70% | 0.76 ± 0.04 ± 0.05 | 0.54 | 0.70 | 712 ± 57 ± 23 | 30.7/10 | 234 |
| $\bar{p}$ | $y = 0$ | 0%–10% | 6.0 ± 0.17 ± 0.38 | 4.3 | 0.70 | 906 ± 38 ± 29 | 15.9/9 | 338 |
| | | 10%–30% | 3.5 ± 0.11 ± 0.22 | 2.4 | 0.69 | 880 ± 12 ± 28 | 3.9/9 | 323 |
| | | 30%–50% | 1.5 ± 0.04 ± 0.10 | 1.0 | 0.68 | 839 ± 16 ± 27 | 7.7/9 | 300 |
| | | 50%–70% | 0.6 ± 0.02 ± 0.04 | 0.38 | 0.64 | 781 ± 22 ± 25 | 10.9/9 | 269 |
| | $y = 3$ | 0%–10% | 1.2 ± 0.04 ± 0.07 | 0.73 | 0.62 | 750 ± 20 ± 24 | 11.7/9 | 254 |
| | | 10%–30% | 0.86 ± 0.04 ± 0.05 | 0.53 | 0.61 | 731 ± 31 ± 23 | 17.1/9 | 244 |
| | | 30%–50% | 0.37 ± 0.01 ± 0.02 | 0.22 | 0.60 | 719 ± 27 ± 23 | 14.2/9 | 238 |
| | | 50%–70% | 0.15 ± 0.01 ± 0.01 | 0.09 | 0.57 | 685 ± 42 ± 22 | 18.2/9 | 221 |

to be the nuclear radius. In Eq. (5), $n(r)$ is the radial density profile. In this analysis $n(r)$ is assumed to have a Gaussian form $\sim e^{-\frac{r^2}{2R^2}}$ for $r < R_{\rm max}$ where $R_{\rm max} = 3R$. For $r > R_{\rm max}$, $n(r) = 0$. The modified Bessel function $K_1(z)$ comes from integration from $-\infty$ to $+\infty$ over pseudorapidity $\eta$ assuming boost invariance. At forward rapidity, the assumption of boost invariance is not valid and $K_1(z)$ should be replaced by an integral over a finite range of $\eta$ so that

$$\frac{dN}{dym_T dm_T} \sim \int_0^{R_{\rm max}} dr\{r \times n(r) \times [m_T I_0(x) g(z)]\}, \quad (6)$$

where

$$g(z) = \int_{\eta_{\rm min}}^{\eta_{\rm max}} \cosh(\eta - y) e^{-z\cosh(\eta - y)} d\eta, \quad (7)$$

and $y$ is the rapidity variable. The limits of the integration in Eq. (7) were $\eta_{\rm min} = 2.4$ and $\eta_{\rm max} = 4.4$. At these limits the integrand in Eq. (7) is very small compared to its central value at $\eta = 3$. The results of the fit are stable with respect to small changes in these limits.

For both the mid-rapidity and forward-rapidity data, we performed a simultaneous fit of the pion, kaon, and (anti)proton spectra with three parameters: $T_{\rm kin}, \beta_s$, and $\alpha$. The normalization parameters are adjusted such that the integral yield of the data in the fitting range is reproduced. Feed down from resonances was not considered because the data do not extend below 0.4 GeV/$c$ where such effects are likely to be significant. The fit ranges for pions, kaons, and protons are restricted to $p_T < 1.8$ GeV/$c$, $p_T < 2.0$ GeV/$c$, and $p_T < 3.0$ GeV/$c$, respectively, because hard processes are expected to become significant above these momenta.

The fits are shown as lines in Fig. 2. The solid lines indicate the transverse mass range for the fits and the dotted lines are extrapolations of the functions beyond the fit range. The systematic errors on the parameters were estimated by changing the fit ranges used for the fits, using different density profiles, and different maximum radii, and for the forward data changing the limits of the $\eta$ integration. The blast wave fit parameters are tabulated in Table VI. The $\frac{dN}{dy}$ and $\langle p_T \rangle$ from the blast wave fit are in reasonable agreement with fits to the individual kaon and proton spectra listed in Tables IV and V.

Figure 3 shows the (anti)correlation between the kinetic temperature $T_{\rm kin}$, and the average transverse velocity $\langle\beta\rangle = \frac{2}{\alpha+2}\beta_s$, for the four centrality classes at both rapidities. As collisions become more central (going from left to right in Fig. 3), $T_{\rm kin}$ decreases as $\langle\beta\rangle$ increases. This is expected because a larger system should stay together for a longer time. As the system cools random thermal motion of the partons is converted to bulk radial flow, lowering the temperature and increasing the average velocity.

At $y = 3$ the slope of the $T_{\rm kin}$ versus $\langle\beta\rangle$ curve is similar to that at $y = 0$, but for a given $\langle\beta\rangle$ the temperatures are about 20 MeV lower. This effect does not just result from having lower particle densities at $y = 3$. Figure 4 shows the dependence of the kinetic freeze-out temperature and the mean radial flow velocity for Cu+Cu and Au+Au collisions as a function of the total $dN/dy$ ($\pi^{\pm}, K^{\pm}, p$, and $\bar{p}$) of each centrality class at a given rapidity. For a given $dN/dy$ both $T_{\rm kin}$ and $\langle\beta\rangle$ are smaller at $y = 3$ reflecting the lower energy (and hence lower $\langle p_T \rangle$) that is available to the matter at forward rapidity. At mid-rapidity the dependence of $T_{\rm kin}$ and $\langle\beta\rangle$ on $dN/dy$ is similar in Cu+Cu and Au+Au reactions, with slightly higher values of $T_{\rm kin}$ and slightly lower values of $\langle\beta\rangle$ in Cu+Cu compared to Au+Au reactions. At mid-rapidity the STAR collaboration has made blast wave fits to $\pi^{\pm}, K^{\pm}$, proton, and antiproton spectra [28]. The reported values for $T_{\rm kin}$ are slightly lower but consistent within errors to the corresponding BRAHMS results. The $p_T$ ranges for the data and fits were also slightly different.

In Fig. 5 the $dN/dy$ values per participant pair are shown for central (left) and forward (right) rapidity for Cu+Cu and Au+Au (mid-rapidity only) collisions [23]. For clarity, only the positive pions and kaons are shown, but the trends are very similar for the corresponding negative particles. At both central

TABLE VI. Blast wave fit parameters, for Cu+Cu collisions at $\sqrt{s_{NN}} = 200$ GeV at various centralities at $y = 0$ (top) and $y = 3$ (bottom). The errors listed are statistical only. The systematic errors are of the order of 5 MeV for $T_{\rm kin}$ and 0.015 for $\langle\beta\rangle$.

| $y = 0$ | | | | |
|---|---|---|---|---|
| Cent. | $T_{\rm kin}$(MeV) | $\langle\beta\rangle$ | $\alpha$ | $\chi^2$/dof |
| 0%–10% | $128 \pm 3$ | $0.501 \pm 0.010$ | $0.499 \pm 0.024$ | 0.84 |
| 10%–30% | $138 \pm 3$ | $0.455 \pm 0.012$ | $0.604 \pm 0.028$ | 1.00 |
| 30%–50% | $149 \pm 4$ | $0.386 \pm 0.018$ | $0.794 \pm 0.045$ | 1.15 |
| 50%–70% | $158 \pm 5$ | $0.303 \pm 0.035$ | $1.16 \pm 0.11$ | 2.63 |
| $y = 3$ | | | | |
| Cent. | $T_{\rm kin}$(MeV) | $\langle\beta\rangle$ | $\alpha$ | $\chi^2$/dof |
| 0%–10% | $127 \pm 1$ | $0.384 \pm 0.004$ | $0.723 \pm 0.011$ | 1.35 |
| 10%–30% | $141 \pm 2$ | $0.327 \pm 0.003$ | $0.886 \pm 0.014$ | 1.61 |
| 30%–50% | $138 \pm 2$ | $0.291 \pm 0.007$ | $1.09 \pm 0.02$ | 1.22 |
| 50%–70% | $160 \pm 3$ | $0.206 \pm 0.006$ | $1.53 \pm 0.03$ | 1.27 |

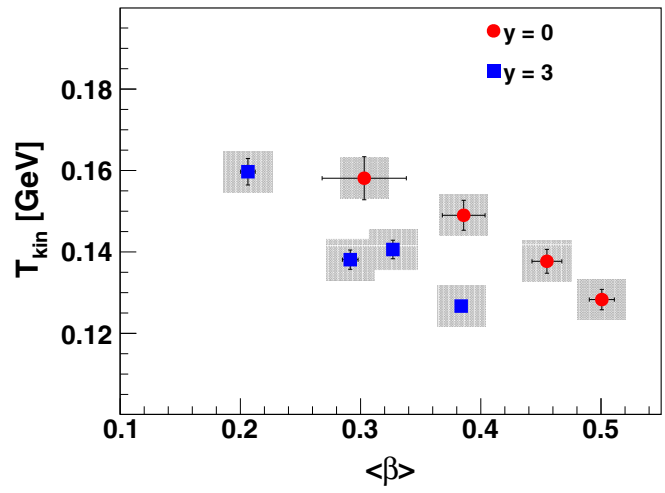


FIG. 3. Blast wave fit parameters $T_{\rm kin}$ vs $\langle\beta\rangle$ for Cu+Cu collisions at $\sqrt{s_{NN}} = 200$ GeV at $y = 0$ (red circles) and $y = 3$ (blue squares). The statistical errors are represented by bars and the systematic errors by the gray boxes. More central collisions are to the right. The numerical values are listed in Table VI.

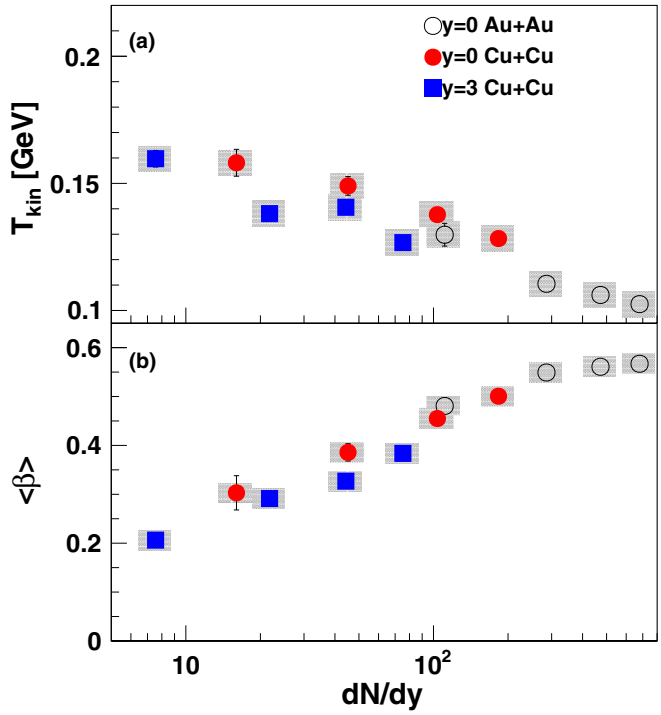


FIG. 4. $T_{\rm kin}$ (top) and $\langle\beta\rangle$ (bottom) for 200 GeV Au+Au collisions at $y = 0$ and Cu+Cu collisions at $y = 0$ and $y = 3$ as a function of total $\frac{dN}{dy}$ ($\pi^{\pm}, K^{\pm}, p$, and $\bar{p}$) for various centralities. The statistical errors are represented by bars and the systematic errors by the gray boxes. The Au+Au spectra used for the fits are from [23].

and forward rapidity the kaon yields per participant pair are somewhat smaller for lower values of $N_{\rm part}$. For $N_{\rm part}$ between 60 and 100 the $\frac{1}{0.5N_{\rm part}}\frac{dN}{dy}$ values for $\pi^{\pm}$ extracted from Cu+Cu collisions are similar to the ones extracted from Au+Au, while for $K^{\pm}$ the scaled $\frac{dN}{dy}$ values are slightly higher. A similar effect was seen by STAR where the $K^-$ and $K^0_S$ yields at a given $N_{\rm part}$ are somewhat higher for Cu+Cu than for Au+Au [19,28].

Beccattini and Manninen have proposed that an increase of the scaled $\frac{dN}{dy}$ values as observed for the kaon yields might reflect the effect of two sources, a chemically equilibrated and dense "core" and a "corona" of independent nucleon-nucleon collisions [9]. As the centrality of the system decreases the ratio of core-to-corona changes causing a change in the kaon yield per participant pair.

Figure 6 shows the average transverse momenta $\langle p_T\rangle$ for pions, kaons, and (anti)protons versus $N_{\rm part}$ for Cu+Cu collisions at $y = 0$ and $y = 3$ and for Au+Au collisions at $y = 0$ [23]. A general observation is that $\langle p_T\rangle$ depends strongly on particle mass, reflecting the larger boost given to the heavier particles by radial flow (as expected from the blast wave model). While the pion $\langle p_T\rangle$ values at $y = 3$ are similar to those at $y = 0$, the kaons and (anti)protons exhibit smaller values at forward rapidity. This drop in $\langle p_T\rangle$ for the heavier particles reflects the lower radial flow and freeze-out temperatures at forward rapidity shown in Figs. 3 and 4.

At mid-rapidity there is a small increase in the pion $\langle p_T\rangle$ as the collisions become more central. The increase of the $\langle p_T\rangle$ values for more central collisions is more pronounced for the kaons and the (anti)protons. The pions and kaons show no dependence of $\langle p_T\rangle$ on centrality at forward rapidity while the (anti)proton $\langle p_T\rangle$ appears to increase as the collisions become more central. The Cu+Cu data points join smoothly with those from Au+Au collisions (a similar result was observed by STAR for the $K^{*0}$ in the two colliding systems [30].) This

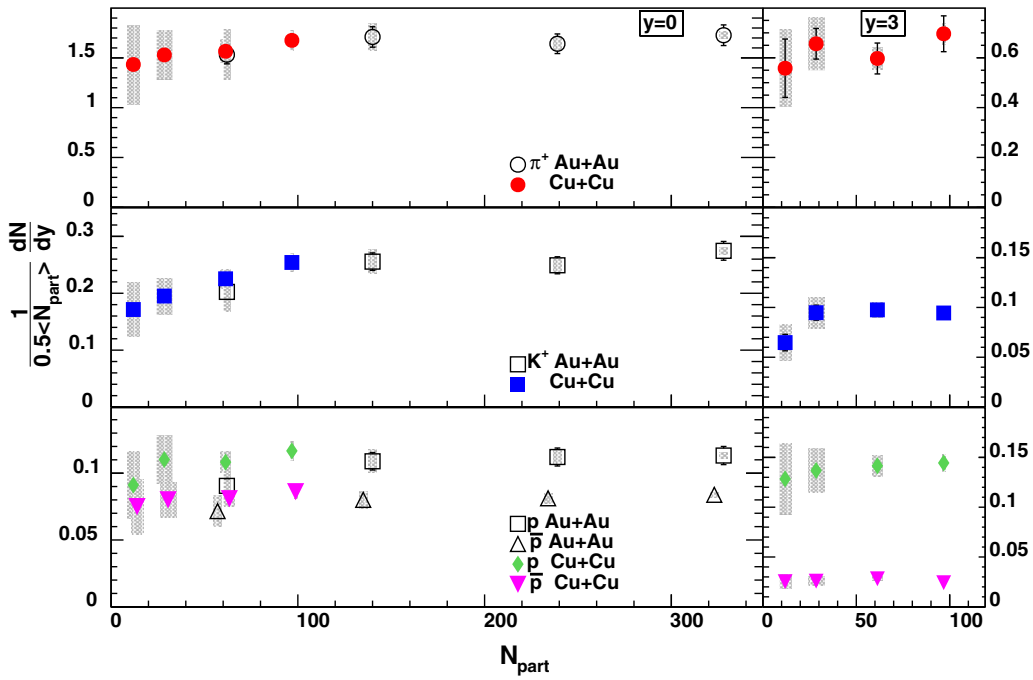


FIG. 5. $\frac{dN}{dy}$ scaled by $N_{\rm part}$ for $\pi^+, K^+$, and proton and antiprotons from Cu+Cu (solid symbols) and Au+Au collisions (open symbols) at $\sqrt{s_{NN}} = 200$ GeV as a function of $N_{\rm part}$ for $y = 0$ (left) and $y = 3$ (right). The Au+Au data are from [23]. The statistical errors are represented by bars and the systematic errors by the gray boxes. The Au+Au pion yields were deduced using a power law extrapolation at low $p_T$.

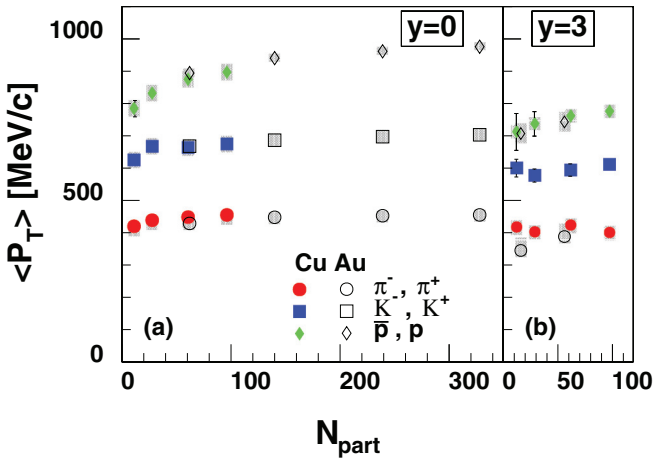


FIG. 6. Mean transverse momentum $\langle p_T \rangle$ for $\pi^{\pm}, K^{\pm}$, $p$, and $\bar{p}$ as a function of $N_{\rm part}$ for Cu+Cu and Au+Au collisions at $\sqrt{s_{NN}} =$ 200 GeV for $y = 0$ (left) and $y = 3$ (right). The statistical errors are represented by bars and the systematic errors by the gray boxes. The Au+Au mid-rapidity data are from [23], and the forward Au+Au proton and pion preliminary data from [29].

suggests that the $\langle p_T \rangle$ values are insensitive to the difference in shape of the Cu+Cu and Au+Au overlap regions for the same number of participants.

### B. Nuclear modification factors

The discovery of high $p_T$ hadron suppression at central rapidity in $\sqrt{s_{NN}} = 130$ GeV Au+Au collisions at RHIC was one of the most exciting results in heavy-ion physics [31–34]. These first measurements have since been extended to higher energies and a broad range of colliding systems, both light and heavy, and also refined to include identified hadrons, heavy quarks, and fully reconstructed jets [35–41]. No such effects have been seen at $y \sim 0$ in d-Au collisions at RHIC [33,34,42,43] confirming that the observed suppression found at mid-rapidity in central heavy-ion collisions is indeed a final-state effect and is specifically a consequence of the energy loss of partons. At forward rapidity, the colliding systems d+Au and Au+Au at $\sqrt{s_{NN}}$ both exhibit high $p_T$ suppression similar to each other and to the mid-rapidity Au+Au results [44].

The nuclear effects on particle production are studied in terms of the nuclear modification factor $R_{AA}$ defined as

$$R_{AA} = \frac{d^2N_{AA}/dp_T dy}{\langle \mathrm{N_{coll}} \rangle d^2N_{pp}/dp_T dy}, \tag{8}$$

which is the ratio of the particle yield in heavy-ion collisions to the yield in $p + p$ collisions scaled by the average number of binary nucleon-nucleon collisions $\langle N_{\rm coll} \rangle$ for a given centrality class. If $AA$ collisions were just a superposition of elementary collisions between nucleons, then $R_{AA}$ should be 1.0 in the $p_T$ region dominated by hard processes.

Partonic energy loss in a hot QGP will typically lead to an $R_{AA}$ value well below unity. Initial-state effects, such as shadowing of the nuclear parton distribution functions may also influence the $R_{AA}$ values and are believed to contribute to the suppression observed at forward rapidity in $\sqrt{s_{NN}} =$ 200 GeV d+Au and Au+Au collisions at RHIC [44,45]. The particle species dependencies of $R_{AA}$ at low to intermediate $p_T$ may be influenced by various medium effects such as collective radial flow (leading to a mass ordering of the $R_{AA}$ of identified hadrons) and/or parton recombination effects (typically leading to meson-baryon differences).

Figure 7 shows the nuclear modification factor $R_{AA}$ for pions, kaons, and (anti)protons, respectively, in Cu+Cu collisions. The pion and kaon $R_{AA}$ values are averages of the positive and negative particles. A general trend immediately seen is the clear mass ordering of the $R_{AA}$ values for the various particle species, most pronounced in the more central collisions and compatible with radial flow and/or recombination effects influencing the modification pattern.

For $1 < p_T < 2\,\mathrm{GeV}/c$ the pions are suppressed at both rapidities for central and mid-central events. The level of suppression is strongest for more central collisions which achieve the highest densities and largest volumes. This is consistent with the fact that the multiplicity density decreases as one goes to more peripheral collisions; there is less matter to interact with and more partons make it out of the collision region before losing much of their energy. Interestingly, the suppression is stronger at forward rapidities where one would expect parton energy loss to be less. This is consistent with the pattern seen for $\pi^-$ mesons in Au+Au collisions [45].

Kaons with $1 < p_T < 2$ GeV/$c$ do not show significant suppression at $y = 0$ but they are suppressed at $y = 3$. The suppression of the kaons is less pronounced than that of the pions but shows a similar dependence on centrality. The difference in the pion and kaon suppression patterns may reveal information about their respective fragmentation functions [46]. At mid-rapidity, the $R_{AA}$ values for pions and kaons vary little with $p_T$ over the range $p_T = 1.5$–$2.5\,\mathrm{GeV}/c$. At forward rapidity there is an increase of the kaon and pion $R_{AA}$ values with $p_T$ similar for all centralities but somewhat less pronounced for the most peripheral sample.

For both protons and antiprotons $R_{AA}$ rises steadily with $p_T$ crossing 1.0 at $p_T \approx 1.3\,\mathrm{GeV}/c$ for all centralities and both rapidities. The enhancement for $p_T > 1.3\,\mathrm{GeV}/c$ is strongest in peripheral collisions and at forward rapidity. At central rapidity, the enhancement is similar for protons and antiprotons but at $y = 3$ the antiprotons show a greater enhancement than the protons, partially because of the isospin-related difference in reference spectra for protons and antiprotons at forward rapidity in $p + p$ collisions [47].

Note that the STAR collaboration has measured $R_{AA}$ for pions and $p + \bar{p}$ at mid-rapidity and $p_T \gtrsim 3\,\mathrm{GeV}/c$ in Cu+Cu collisions at $\sqrt{s_{NN}} = 200$ GeV/$c$ [48]. The STAR results are consistent with our highest $p_T$ data points but fall steadily before leveling off at $p_T \approx 6\,\mathrm{GeV}/c$.

To improve the statistical precision of the results, the Cu+Cu and $p + p$ spectra were summed over the $p_T$ region 1.3–2.5 GeV/$c$ and the $\pi^{\pm}$ and $K^{\pm}$ spectra averaged before taking the ratio shown in Eq. (8). The resulting $R_{AA}$ values as a function of $N_{\rm part}$ are shown in Fig. 8. For pions and kaons the $R_{AA}$ values are smaller at $y = 3$ than at $y = 0$, for protons they are similar at the two rapidities, while for antiprotons the $R_{AA}$ values are larger at $y = 3$ than at $y = 0$. For pions and kaons

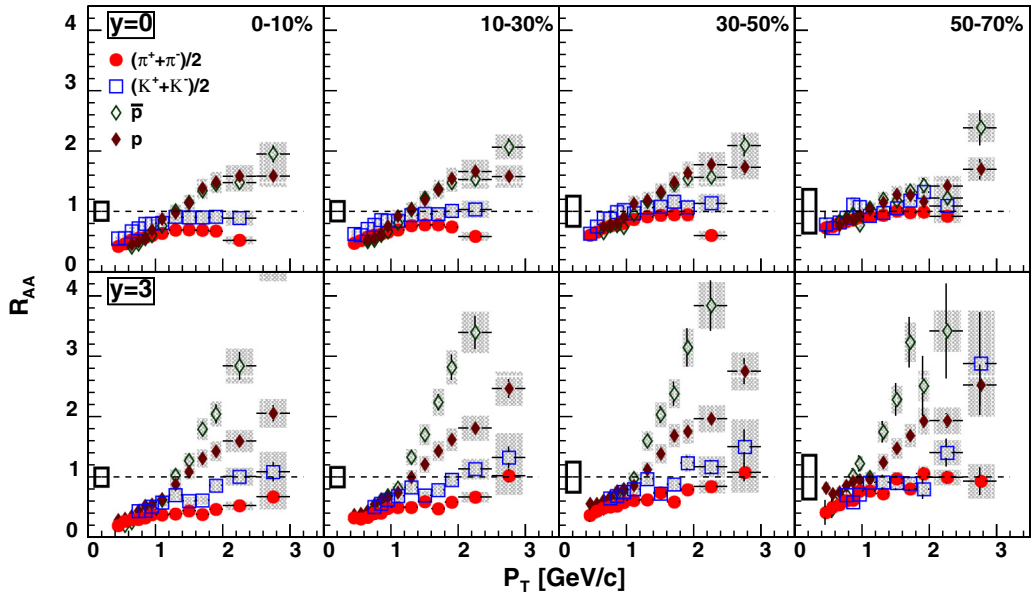


FIG. 7. Nuclear modification factor of $\sqrt{s_{NN}} = 200$ GeV Cu+Cu collisions for pions, kaons, and (anti)protons as a function of $p_T$ and centrality. The top row is for $y = 0$ and the bottom row $y \approx 3$. The centrality decreases from left to right. The statistical errors are represented by bars and the systematic errors by the gray boxes. The white boxes at $p_T = 0$ represent the correlated systematic normalization uncertainty from the $p + p$ reference and the error on the number of binary collisions.

$R_{AA}$ drops with $N_{\rm part}$ at both $y = 0$ and $y = 3$, while this trend is less clear for the baryons. For both protons and antiprotons $R_{AA}$ is above 1.0 for all values of $N_{\rm part}$ and at both rapidities, with antiprotons at $y = 3$ standing out as most enhanced and with $R_{AA}$ falling with $N_{\rm part}$.

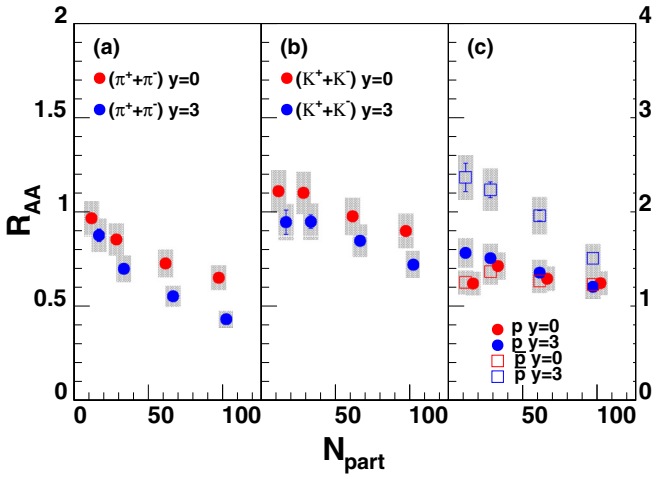


FIG. 8. Nuclear modification factor of $\sqrt{s_{NN}} = 200$ GeV Cu+Cu collisions for the $p_T$ region 1.3–2.5 GeV/$c$ for pions (left), kaons (center), and (anti)protons (right) as a function of $N_{\rm part}$ for $y = 0$ (red symbols) and $y = 3$ (blue symbols). Systematic errors are shown by the gray bands. However, the systematic errors that arise from uncertainties in $N_{\rm coll}$ and the pp normalization are common to the $y = 0$ and $y \approx 3$ data sets and so are not included. These errors are listed in Table I. Note the different vertical scale for the (anti)proton $R_{AA}$.

The fact that the mesons are more strongly suppressed for more central collisions is expected from models of parton energy loss or jet quenching. In such models it is expected that the energy loss should be less at forward rapidities because of the decreasing particle density. However, this effect my be compensated in the $R_{AA}$ ratio by a relative softening of the Cu+Cu $p_T$ spectra at forward rapidities. PHENIX has suggested that a similar effect may explain why at high $p_T$ $R_{AA}$ is almost the same at $\sqrt{s_{NN}} = 63$ and 200 GeV [49]. It is also possible that at forward rapidity initial state effects such as nuclear shadowing reduce particle production [44,45].

### C. Particle ratios

Figure 9 shows antiparticle to particle $\frac{dN}{dy}$ ratios of integrated yields measured in Cu+Cu and Au+Au collisions at $\sqrt{s_{NN}} = 200$ GeV as a function of $N_{\rm part}$, for $y = 0$ and $y \sim 3$. These ratios of integrated yields do not exhibit a centrality dependence at mid-rapidity. There is very little difference between the Cu+Cu and Au+Au results. At $y = 3$ there is a slight drop of the $\frac{\pi^-}{\pi^+}$ ratio with $N_{\rm part}$.

Figure 10 shows the kaon to pion ratios (upper two panels) and proton to meson ratios (lower two panels) as functions of $p_T$, centrality, and rapidity. At mid-rapidity, the $\frac{K}{\pi}$ ratios show a linear increase at low $p_T$ but increase less rapidly for $p_T > 1.5$ GeV/$c$, with the $\frac{K^+}{\pi^+}$ ratio showing only a slight excess over the corresponding $\frac{K^-}{\pi^-}$ values. At $y = 3$, both $\frac{K}{\pi}$ ratios show a slightly stronger centrality dependence than at $y = 0$, and the $K^+/\pi^+$ ratios are significantly enhanced over the corresponding $K^-/\pi^-$ results.

Both the $\frac{p}{\pi^+}$ and $\frac{\bar{p}}{\pi^-}$ ratios increase with $p_T$ at both rapidities with saturation taking place at $p_T \sim 1.6$ GeV/$c$

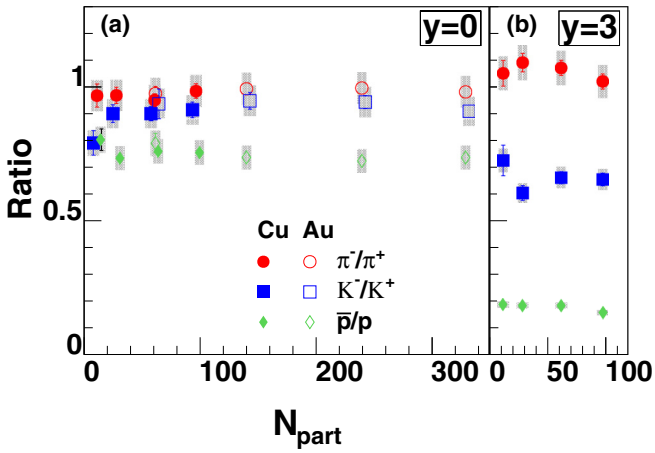


FIG. 9. Ratios of antiparticle-particle yields versus $N_{\rm part}$ for pions, kaons, and protons at $y = 0$ (left) for Cu+Cu (solid symbols) and Au+Au (open symbols) collisions and (right) for Cu+Cu collisions at $y = 3$. Both Cu+Cu and Au+Au collisions are at $\sqrt{s_{NN}} = 200$ GeV. The statistical errors are represented by bars and the systematic errors by the gray boxes.

for $y = 3$. The baryon-meson ratios also show a moderate centrality dependence at the two rapidities. Both ratios at this $\langle p_T \rangle$ range exceed the maximum value of 0.2 observed from the fragmentation of both quark and gluon jets in $e^+e^-$ collisions at $\sqrt{s} = 91.2$ GeV [50,51]. Various mechanisms such as quark coalescence, radial flow or baryon transport dynamics may boost the baryon-meson ratios at intermediate $p_T$ above the expected fragmentation value [52–62]. At mid-rapidity, the $p_T$ dependence of the BRAHMS $\frac{p}{\pi^+}$ ratio in central Au+Au collisions at $\sqrt{s_{NN}} = 200$ GeV [63] was reasonably described by recombination [56,59,64–67] and hydrodynamical models [68]. Hydrodynamic models also qualitatively reproduced the trend [53–55]. Although it is clear that the system size and the chemical properties of the medium are important parameters, the detailed behavior of hadron production in the forward rapidity region remains a challenge to microscopic models, as also seen in Ref. [69].

The $N_{\rm part}$ dependence of the $\frac{K}{\pi}$ and $\frac{p}{\pi}$ ratios is displayed in Fig. 11. Here the individual spectra have been integrated over the $p_T$ range 1.3–2.0 GeV/$c$ for $y = 0$ and over 1.5–3.0 GeV/$c$ for $y = 3$. We also show the ratios obtained from the BRAHMS $p + p$ data [47,70]. The $p + p$ values fit smoothly with the trend of the lower $N_{\rm part}$ values for Cu+Cu. The $\frac{K}{\pi}$ ratios increase slightly with $N_{\rm part}$, with the strongest centrality dependence seen for peripheral collisions at $y = 3$. The $\frac{K^+}{\pi^+}$ ratios are significantly larger than the $\frac{K^-}{\pi^-}$ ratios at $y = 3$, but the two ratios are similar at $y = 0$. This may be attributed to the

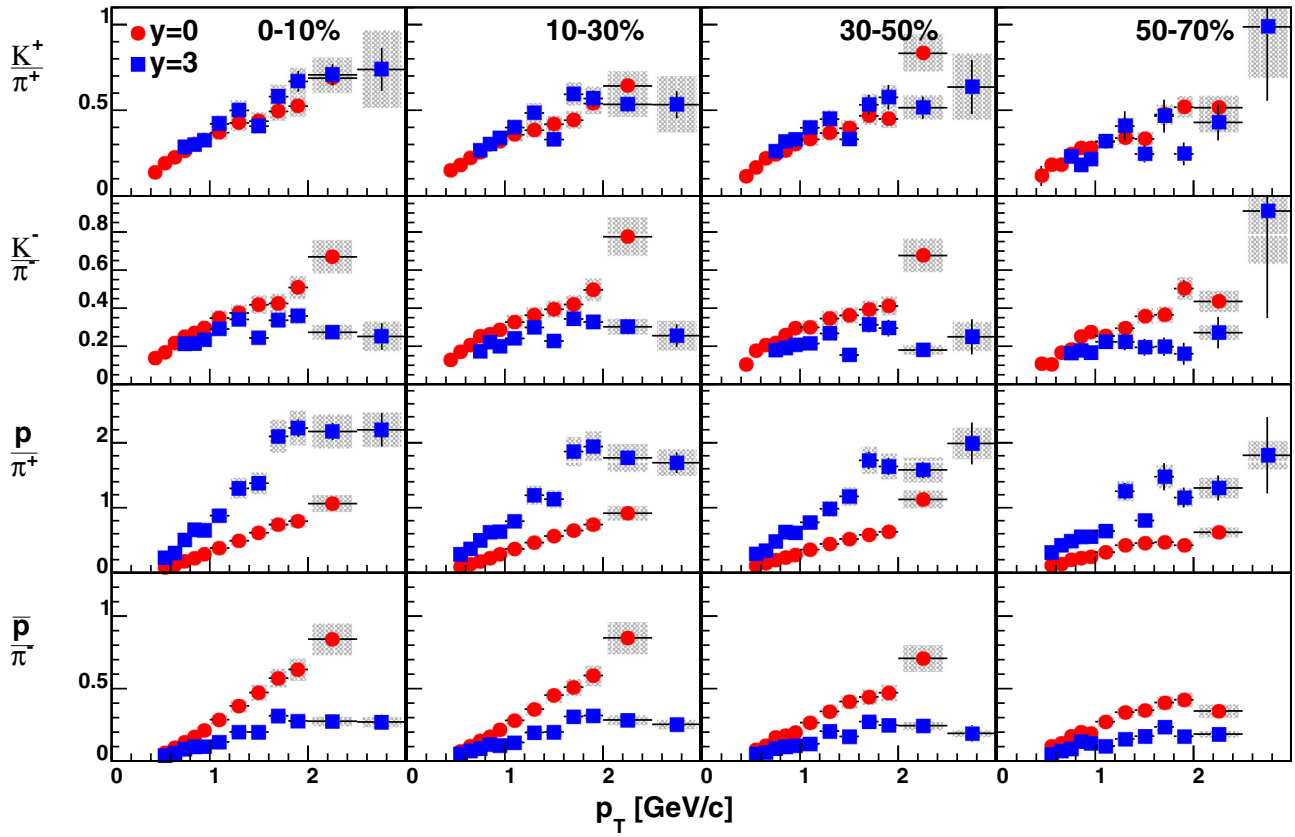


FIG. 10. Particle ratios from Cu+Cu collisions at $\sqrt{s_{NN}} = 200$ GeV as a function of $p_T$, at $y = 0$ (red circles) and $y = 3$ (blue squares) for various centralities. The centrality decreases from left to right. The statistical errors are shown by bars and the systematic errors by the gray boxes. The systematic errors include the point-to-point uncertainties, and the PID uncertainties, but not the overall normalization that cancels for these ratios.

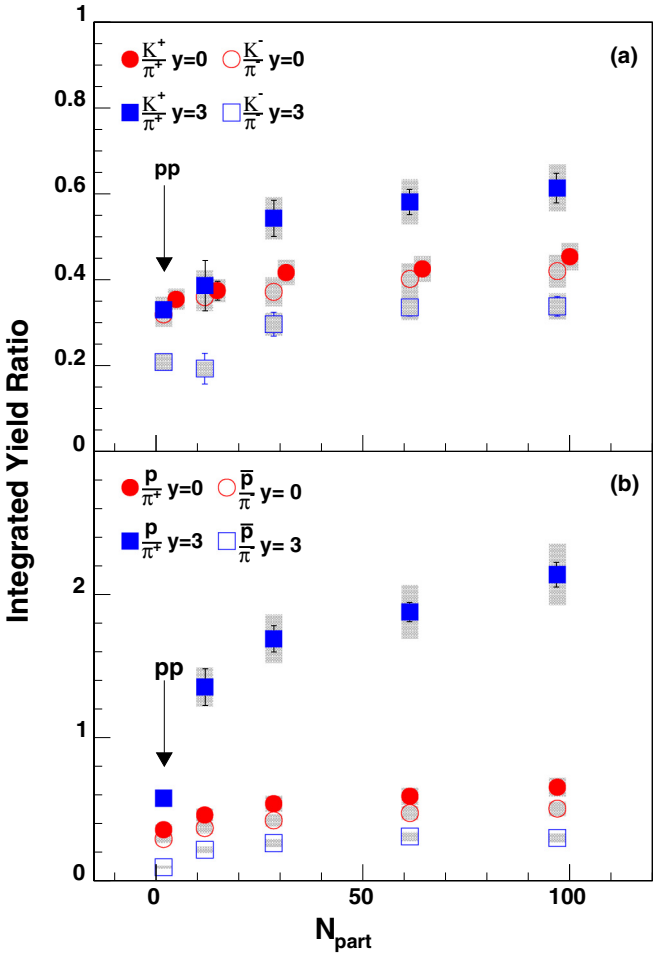


FIG. 11. Ratio of particle yields, $\frac{K}{\pi}$ (top) and (bottom) $\frac{p}{\pi}$ as a function of $N_{\rm part}$ for Cu+Cu and pp collisions at $\sqrt{s_{NN}} = 200$ GeV. The pp data are at $N_{\rm part} = 2$ and are indicated by the arrows. Before division the individual spectra have been integrated over $1.3 < p_T < 2.0$ GeV/$c$ for $y = 0$ and over $1.5 < p_T < 3.0$ GeV/$c$ for $y = 3$. Red circles denote $y = 0$ and blue squares $y = 3$. Solid symbols represent ratios of positive particles while open symbols show the ratios of negative particles. The statistical errors are shown by bars while the systematic errors are shown by gray boxes. Note that the $\frac{K^+}{\pi^+}$ ratios at $y = 0$ are displaced slightly horizontally for clarity.

larger baryon density at $y = 3$ which increases the probability of associated production for $K^+$.

The bottom panel of Fig. 11 shows the integrated $\frac{p}{\pi^+}$ and $\frac{\bar{p}}{\pi^-}$ ratios versus $N_{\rm part}$. The ratios seem to exhibit a monotonic increase with $N_{\rm part}$ at both rapidities. Again the pp ratios fit the trend of the lower $N_{\rm part}$ results but this dependence is stronger at $y = 3$. At mid-rapidity the ratios are smaller than unity with $\frac{p}{\pi^+}$ values slightly larger than the corresponding $\frac{\bar{p}}{\pi^-}$ values. At forward rapidity, the $\frac{p}{\pi^+}$ ratio is generally greater than unity and is larger than the corresponding $\frac{\bar{p}}{\pi^-}$ ratio by almost a factor of 6. This was also observed in Au+Au collisions at the same center-of-mass energy per nucleon [20]. While the beam protons may be contributing to the $\frac{p}{\pi^+}$ ratio, the reason for such large differences between the positive and negative baryon-to-meson ratios is not yet well understood. The increase of the baryon-to-meson ratios with centrality is consistent with trends exhibited by the $R_{AA}$ values, where mesons become more suppressed for central events while baryons show only a weak if any centrality dependence.

## IV. SUMMARY AND CONCLUSIONS

The $\pi^{\pm}, K^{\pm}, p$, and $\bar{p}$ spectra from Cu+Cu collisions at $\sqrt{s_{NN}} = 200$ GeV are well described by blast wave fits at both central and forward rapidities. As $N_{\rm part}$ increases the kinetic temperature $T_{\rm kin}$ drops and the mean velocity $\langle\beta\rangle$ rises. For a given $\langle\beta\rangle$, $T_{\rm kin}$ is about 15–20 MeV smaller at $y = 3$ than at $y = 0$. The particle yields per participant pair increase with $N_{\rm part}$. For a given $N_{\rm part}$ the kaon $dN/dy$ values are slightly larger in Cu+Cu collisions than in Au+Au collisions.

Both pions and kaons from Cu+Cu collisions are suppressed relative to scaled $p + p$ collisions. The suppression is strongest for central collisions as expected from models of parton energy loss or jet quenching. The suppression is slightly stronger at forward rapidity than at central rapidity suggesting that the effect of the hot and dense medium extends to at least $y \approx 3$ at RHIC energies. This is despite the fact that the rapidity densities in the forward region are about half of those at mid-rapidity. The PHENIX collaboration has observed that increasing parton energy loss with increasing beam energy can be compensated by hardening of the $p_T$ spectra, in such a way that $R_{AA}$ remains unchanged [49]. A similar effect may be present when going to forward rapidities, so that the approximately constant $R_{AA}$ can be a result of reduced energy loss combined with steeper $p_T$ spectra for mesons. It is also possible that initial state effects such as nuclear shadowing are affecting particle production at forward rapidities [44,45].

In contrast to the pions and kaons, protons with $p_T > 1.3$ GeV/$c$ are enhanced relative to scaled $p + p$ collisions. The baryon enhancement seen in $R_{AA}$ depends strongly on $p_T$ and rapidity but only weakly on centrality. The enhancement is similar for protons and antiprotons at $y = 0$, but is stronger for antiprotons at forward rapidity. This is mainly because the $p + p$ reference spectrum for antiprotons at $y = 3$ is much steeper than the corresponding proton spectrum [47].

The $\frac{\pi^-}{\pi^+}, \frac{K^-}{K^+}$ and $\frac{\bar{p}}{p}$ ratios are almost independent of $p_T$ and centrality but they do depend upon rapidity, presumably because of the higher net-baryon density in the forward region. The $\frac{K^{\pm}}{\pi^{\pm}}, \frac{p}{\pi^+}$, and $\frac{\bar{p}}{\pi^-}$ ratios increase with $N_{\rm part}$ for $p_{\rm T}$ up to $\simeq$1.6–2 GeV/$c$ at both rapidities. The four ratios at $y = 3$ are seen to saturate for $p_T \geqslant 1.6$ GeV/$c$. At $y = 3$, the kaon-pion and proton-pion ratios exhibit a slightly different centrality dependence in the lowest $N_{\rm part}$ region.

At both rapidities the $\frac{p}{\pi^+}$ and $\frac{\bar{p}}{\pi^-}$ ratios in the intermediate $p_T$ region, i.e., 2.0 GeV/$c$ $< p_T <$ 3.5 GeV/$c$ are somewhat larger for central collisions. This may be explained by either quark coalescence [52,56–59], radial flow [53–55], or baryon transport dynamics based on topological gluon field configurations [60–62]. A similar baryon enhancement was observed for Pb+Pb collisions at $\sqrt{s_{NN}} = 2.76$ TeV [71]. These

data are also consistent with recombination [56,59,64–67] and hydrodynamical models [68].

Understanding the underlying mechanisms responsible for hadron production over the broad range of transverse momentum and rapidity accessible at RHIC and providing a consistent description of all the various aspects of the hadron spectra in heavy-ion collisions remains a major challenge. The current data will help constrain theoretical attempts to reach such a synthesis.

## ACKNOWLEDGMENTS

This work was supported by the Office of Nuclear Physics within the U.S. DOE Office of Science, the Danish Natural Science Research Council, the Carlsberg Foundation and the Danish National Research Foundation, the Research Council of Norway, the Polish State Committee for Scientific Research (KBN), and the Romanian Ministry of National Education and Scientific Research.

[1] P. K. Kovtun, D. T. Son, and A. O. Starinets, Phys. Rev. Lett. **94**, 111601 (2005).
[2] I. Arsene *et al.* (BRAHMS Collaboration), Nucl. Phys. **A757**, 1 (2005).
[3] K. Adcox *et al.* (PHENIX Collaboration), Nucl. Phys. **A757**, 184 (2005).
[4] B. Back, M. Baker, M. Ballintijn, D. Barton, B. Becker *et al.* (PHOBOS Collaboration), Nucl. Phys. **A757**, 28 (2005).
[5] J. Adams *et al.* (STAR Collaboration), Nucl. Phys. **A757**, 102 (2005).
[6] S. Adler *et al.* (PHENIX Collaboration), Phys. Rev. C **69**, 034909 (2004).
[7] A. Adare *et al.* (PHENIX Collaboration), Phys. Rev. C **88**, 024906 (2013).
[8] K. Werner, Phys. Rev. Lett. **98**, 152301 (2007).
[9] F. Becattini and J. Manninen, Phys. Lett. B **673**, 19 (2009).
[10] F. Abe *et al.* (CDF Collaboration), Phys. Rev. Lett. **61**, 1819 (1988).
[11] S. S. Adler *et al.* (PHENIX Collaboration), Phys. Rev. C **69**, 034910 (2004).
[12] A. Adare *et al.* (PHENIX Collaboration), Phys. Rev. D **76**, 051106 (2007).
[13] M. Adamczyk *et al.* (BRAHMS Collaboration), Nucl. Instrum. Meth. A **499**, 437 (2003).
[14] C. Adler, A. Denisov, E. Garcia, M. J. Murray, H. Strobele *et al.*, Nucl. Instrum. Meth. A **470**, 488 (2001).
[15] R. Debbe, C. E. Jorgensen, J. Olness, and Z. Yin, Nucl. Instrum. Meth. A **570**, 216 (2007).
[16] R. Brun, F. Carminati, and S. Giani, Report No. CERN-W5013, CERN-W-5013, W5013, W-5013 (1994).
[17] I. Bearden *et al.* (BRAHMS Collaboration), Phys. Rev. Lett. **88**, 202301 (2002).
[18] B. I. Abelev *et al.* (STAR Collaboration), Phys. Rev. C **75**, 064901 (2007).
[19] G. Agakishiev *et al.* (STAR Collaboration), Phys. Rev. Lett. **108**, 072301 (2012).
[20] I. Arsene *et al.* (BRAHMS Collaboration), Phys. Lett. B **684**, 22 (2010).
[21] K. Adcox *et al.* (PHENIX Collaboration), Phys. Rev. Lett. **89**, 092302 (2002).
[22] J. Adams *et al.* (STAR Collaboration), Phys. Lett. B **616**, 8 (2005).
[23] I. Arsene *et al.* (BRAHMS Collaboration), Phys. Rev. C **72**, 014908 (2005).
[24] B. Tomasik, U. A. Wiedemann, and U. W. Heinz, Heavy Ion Phys. **17**, 105 (2003).
[25] G. Wilk and Z. Wlodarczyk, Phys. Rev. Lett. **84**, 2770 (2000).
[26] J. Adams *et al.* (STAR Collaboration), Phys. Rev. C **71**, 064902 (2005).
[27] A. Adare *et al.* (PHENIX Collaboration), Phys. Rev. D **83**, 052004 (2011).
[28] M. M. Aggarwal *et al.* (STAR Collaboration), Phys. Rev. C **83**, 034910 (2011).
[29] F. Videbaek (BRAHMS Collaboration), Nucl. Phys. A **830**, 43C (2009).
[30] M. Aggarwal *et al.* (STAR Collaboration), Phys. Rev. C **84**, 034909 (2011).
[31] K. Adcox *et al.* (PHENIX Collaboration), Phys. Rev. Lett. **88**, 022301 (2002).
[32] C. Adler *et al.* (STAR Collaboration), Phys. Rev. Lett. **89**, 202301 (2002).
[33] I. Arsene *et al.* (BRAHMS Collaboration), Phys. Rev. Lett. **91**, 072305 (2003).
[34] B. Back *et al.* (PHOBOS Collaboration), Phys. Lett. B **578**, 297 (2004).
[35] S. Adler *et al.* (PHENIX Collaboration), Phys. Rev. Lett. **91**, 072301 (2003).
[36] J. Adams *et al.* (STAR Collaboration), Phys. Rev. Lett. **91**, 172302 (2003).
[37] A. Adare *et al.* (PHENIX Collaboration), Phys. Rev. Lett. **98**, 172301 (2007).
[38] G. Aad *et al.* (ATLAS Collaboration), Phys. Rev. Lett. **105**, 252303 (2010).
[39] S. Chatrchyan *et al.* (CMS Collaboration), Phys. Rev. C **84**, 024906 (2011).
[40] G. Aad *et al.* (ATLAS Collaboration), Phys. Lett. B **719**, 220 (2013).
[41] S. Chatrchyan *et al.* (CMS Collaboration), J. High Energy Phys. 10 (2012) 087.
[42] S. Adler *et al.* (PHENIX Collaboration), Phys. Rev. Lett. **91**, 072303 (2003).
[43] J. Adams *et al.* (STAR Collaboration), Phys. Rev. Lett. **91**, 072304 (2003).
[44] I. Arsene *et al.* (BRAHMS Collaboration), Phys. Rev. Lett. **93**, 242303 (2004).
[45] I. Arsene *et al.* (BRAHMS Collaboration), Phys. Lett. B **650**, 219 (2007).
[46] M. Djordjevic and M. Djordjevic, J. Phys. G **41**, 055104 (2014).
[47] I. Arsene *et al.* (BRAHMS Collaboration), Phys. Rev. Lett. **98**, 252001 (2007).
[48] B. Abelev *et al.* (STAR Collaboration), Phys. Rev. C **81**, 054907 (2010).
[49] A. Adare *et al.* (PHENIX Collaboration), Phys. Rev. Lett. **109**, 152301 (2012).
[50] P. Abreu *et al.* (DELPHI Collaboration), Eur. Phys. J. C **5**, 585 (1998).
[51] P. Abreu *et al.* (DELPHI Collaboration), Eur. Phys. J. **C17**, 207 (2000).

[52] X.-F. Guo and X.-N. Wang, Phys. Rev. Lett. **85**, 3591 (2000).
[53] T. Hirano and Y. Nara, Phys. Rev. C **68**, 064902 (2003).
[54] T. Hirano and Y. Nara, Phys. Rev. C **69**, 034908 (2004).
[55] U. W. Heinz and P. F. Kolb, Nucl. Phys. A **702**, 269 (2002).
[56] R. C. Hwa and C. B. Yang, Phys. Rev. C **70**, 024905 (2004).
[57] V. Greco, C. M. Ko, and P. Levai, Phys. Rev. C **68**, 034904 (2003).
[58] V. Greco, C. M. Ko, and I. Vitev, Phys. Rev. C **71**, 041901 (2005).
[59] R. J. Fries, B. Muller, C. Nonaka, and S. A. Bass, Phys. Rev. C **68**, 044902 (2003).
[60] I. Vitev and M. Gyulassy, Phys. Rev. C **65**, 041902 (2002).
[61] I. Vitev and M. Gyulassy, Nucl. Phys. A **715**, 779c (2003).
[62] V. Topor Pop, M. Gyulassy, J. Barrette, C. Gale, X. N. Wang, N. Xu, and K. Filimonov, Phys. Rev. C **68**, 054902 (2003).
[63] P. Staszel (BRAHMS Collaboration), Nucl. Phys. A **774**, 77 (2006).
[64] R. J. Fries, B. Muller, C. Nonaka, and S. A. Bass, Phys. Rev. Lett. **90**, 202303 (2003).
[65] R. J. Fries, S. A. Bass, and B. Muller, Phys. Rev. Lett. **94**, 122301 (2005).
[66] C. B. Chiu, R. C. Hwa, and C. B. Yang, Phys. Rev. C **78**, 044903 (2008).
[67] K. C. Han, R. J. Fries, and C. M. Ko, Phys. Rev. C **93**, 045207 (2016).
[68] P. Bozek and I. Wyskiel-Piekarska, Phys. Rev. C **85**, 064915 (2012).
[69] I. Arsene *et al.* (BRAHMS Collaboration), Phys. Lett. B **687**, 36 (2010).
[70] I. C. Arsene *et al.* (BRAHMS Collaboration) (to be published).
[71] B. B. Abelev *et al.* (ALICE Collaboration), Phys. Lett. B **736**, 196 (2014).